JACS
JOURNAL OF THE AMERICAN CHEMICAL SOCIETY
Article
pubs.acs.org/JACS

Reversible Intercalation of Hexagonal Boron Nitride with Brønsted Acids

Nina I. Kovtyukhova,*[,†] Yuanxi Wang,[‡] Ruitao Lv,[‡] Mauricio Terrones,[‡] Vincent H. Crespi,*[,‡] and Thomas E. Mallouk*[,†]

[†]Department of Chemistry and [‡]Department of Physics, The Pennsylvania State University, University Park, Pennsylvania 16802, United States

Supporting Information

ABSTRACT: Hexagonal boron nitride (h-BN) is an insulating compound that is structurally similar to graphite. Like graphene, single sheets of BN are atomically flat, and they are of current interest in few-layer hybrid devices, such as transistors and capacitors, that contain insulating components. While graphite and other layered compounds can be intercalated by redox reactions and then converted chemically to suspensions of single sheets, insulating BN is not susceptible to oxidative intercalation except by extremely strong oxidizing agents. We report that stage-1 intercalation compounds can be formed by simple thermal drying of h-BN in Brønsted acids H_2SO_4, H_3PO_4, and $HClO_4$. X-ray photoelectron and vibrational spectra, as well as electronic structure and molecular dynamics calculations, demonstrate that noncovalent interactions of these oxyacids with the basic N atoms of the sheets drive the intercalation process.

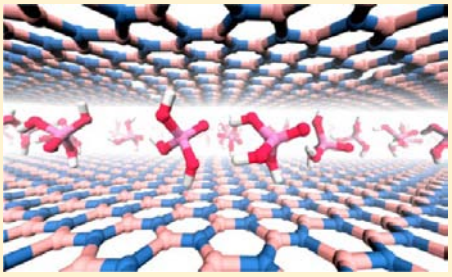

INTRODUCTION

Intercalation reactions of lamellar solids form the basis of a number of practical technologies and are now of increasing interest in the context of physical phenomena that are unique to 2D materials.[1−3] Intercalation reactions are often used as the first step in exfoliation of lamellar crystals to individual atomic/molecular layers.[4−10] In this family of materials, graphene,[11] transition metal dichalogenides,[10,12] and hexagonal boron nitride (h-BN)[13−15] can be mechanically exfoliated to form crystalline, atomically flat semimetallic, semiconducting, and insulating sheets. In order to produce such monolayers as free-standing sheets in practical quantities for device fabrication and physical property measurements, several solution-based chemical approaches have been studied.[10,16−22] Among these, only exfoliation of preformed stage-1 intercalation compounds gives an appreciable yield of single sheets.[10,21−25]

Both graphite and transition metal dichalogenides are amenable to host−guest redox reactions that are sufficiently favorable energetically that they can overcome the van der Waals forces between sheets.[1,2] Intercalation chemistries of graphite and transition metal dichalogenides are thus well developed.[1,3,26,27] As a wide band-gap insulator with polar bonds, the dielectric,[28,29] electrochemical,[30] thermal,[31] and optical[32] properties of BN offer exciting possibilities for devices based on individual sheets and intercalation compounds. However, the large band gap (~5.2 eV) of BN[33,34] and the electrostatic attraction between sheets makes the energetics of redox-driven intercalation unfavorable. The literature on h-BN intercalation chemistry is contradictory with both positive and negative results described.[35−37] Reductive intercalation with potassium has been demonstrated in h-BN thin films,[33] and bulk h-BN has been intercalated at high temperature by Li.[38] The only example of successful oxidative intercalation of h-BN involves the powerful oxidant $S_2O_6F_2$, although intercalation compounds of uncertain composition and structure with SbF_5/F_2 were also reported.[39] Intercalation of strong oxidizing or reducing agents often involves damage to the sheets or formation of host−guest covalent bonds that irreversibly alter the physical and electronic structure of the layers. Well-known examples of this effect are lithiated transition metal disulfides, lithium-intercalated graphite, graphite oxide, and graphite fluorides.[1−3]

Thus, intercalation of molecules through nonspecific, reversible interactions with h-BN sheets remains an unsolved problem, the solution of which could lead to a new family of intercalated layered materials and single-sheet devices.[40,41]

We report here the nonoxidative intercalation of h-BN by Brønsted acids H_2SO_4, H_3PO_4, and $HClO_4$ to form stage-1 intercalation compounds. Spectroscopic data and electronic structure/molecular dynamics calculations indicate that the acids intercalate into h-BN through polar interactions with the layers, especially through hydrogen bonds to the basic nitrogen atoms of the sheets. Spectra also suggest the possibility of polar interactions between the oxygen atoms of the acids and the boron atoms of the h-BN layers.

RESULTS AND DISCUSSION

Intercalation reactions of h-BN occur upon thermal drying of films of h-BN microcrystals drop cast from suspensions of concentrated aqueous acids. Acids of different molecular size, shape, and acid strength were studied: H_2SO_4, H_3PO_4, $HClO_4$,

Received: March 30, 2013
Published: May 10, 2013

   dx.doi.org/10.1021/ja403197h | J. Am. Chem. Soc. 2013, 135, 8372−8381

HCl, HNO_3, CH_3COOH, HCOOH, $C_6H_5SO_3H$, and H_2O. Among these, only H_2SO_4, H_3PO_4, and $HClO_4$ reacted, forming new phases with interplanar spacings of 7.4 , 6.9, and 6.6 Å, respectively. The differences between these distances and the interplanar spacing in h-BN (3.3 Å) indicate average gallery heights of 4.1, 3.6, and 3.3 Å, respectively, and formation of stage-1 intercalation compounds (Figures 1 and 2 and Table S1, Supporting Information). These gallery heights are sufficient to accommodate a single layer of intercalated acid molecules, although by comparison the d_{001} distances in stage-1 graphite intercalation compounds with sulfuric acid are ~1 Å larger (~8 Å).[1] Interestingly, and regardless of the acid/h-BN molar ratio, we have never observed *00l* reflections characteristic of higher stages, which are typical products of graphite intercalation with oxidizing agents. Similar differences between the intercalation behavior of h-BN and graphite were also noted for the intercalation reaction with $S_2O_6F_2$.[39] Several weak reflections, indicating formation of some other as-yet unidentified crystalline phase(s), also appear in the high-angle region of the X-ray diffraction (XRD) patterns of both h-BN/H_2SO_4 and h-BN/H_3PO_4 systems. The pattern of *00l* intensities is different for the three h-BN intercalation compounds and also changes upon drying, which indicates different distributions of electron density in the galleries of the three compounds.

Importantly, there was no evidence of intercalation in the wet films (even after heating for many hours) or in liquid acid suspensions of h-BN (even after several months) that were not subjected to drying. In order to better understand the role of drying in initiating the intercalation reaction, we performed thermal analysis of the starting h-BN/acid suspensions in the isothermal regime. h-BN/H_2SO_4 and h-BN/H_3PO_4 suspensions were heated to 130 and 120 °C, respectively, and kept at these temperatures for 22 h. Results are shown in Figure S1, Supporting Information. Some dehydration of the acids occurs during the first hour, during which they lose 11−12% of their water. After the first hour, the weight of the suspensions decreases more slowly and the ratio of water to acid (H_2SO_4 or H_3PO_4) in the vapor phase becomes constant. The water content of the liquid thus reaches its equilibrium value rapidly and remains constant thereafter. Thus, although dehydration of the acids may be an important driving force in the intercalation reaction, dehydration alone is not sufficient to initiate the reaction. Dehydration is a relatively fast process, and intercalation is found to occur only when the films are heated to dryness.

Dried films acquire a light gray color and are very hygroscopic. In all h-BN/acid systems, the intercalated phases coexist with some amount of intact h-BN, which is less in the h-

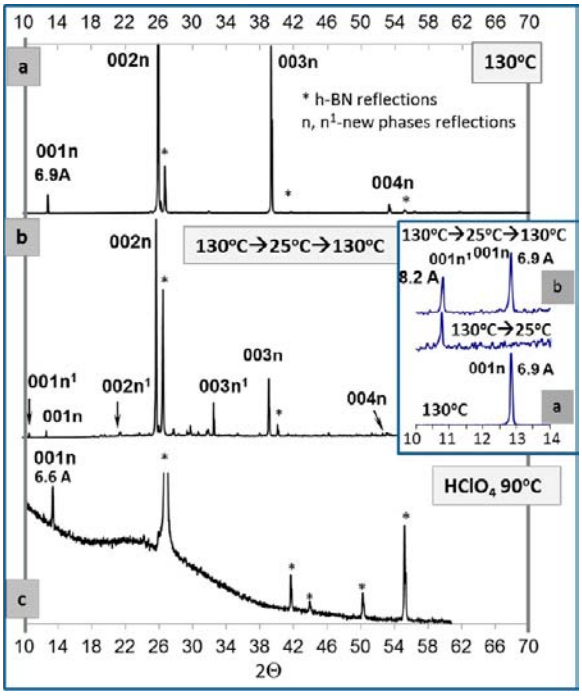

Figure 1. XRD patterns of h-BN/H_2SO_4 (a and b) and h-BN/$HClO_4$ (c) films prepared by (a) drying the suspension at 130 °C and (b) drying at 130 °C (sample A) then exposing to ambient conditions for 3 days and heating again at 130 °C for 1 day. (Inset) Low-angle XRD patterns of sample A (bottom) kept under ambient conditions for 3 days (center) and then heated again at 130 °C for 1 day (top) and (c) drying at 90 °C. The asterisk (*) indicates h-BN reflections; n, n^1 indicate reflections of the new phases.

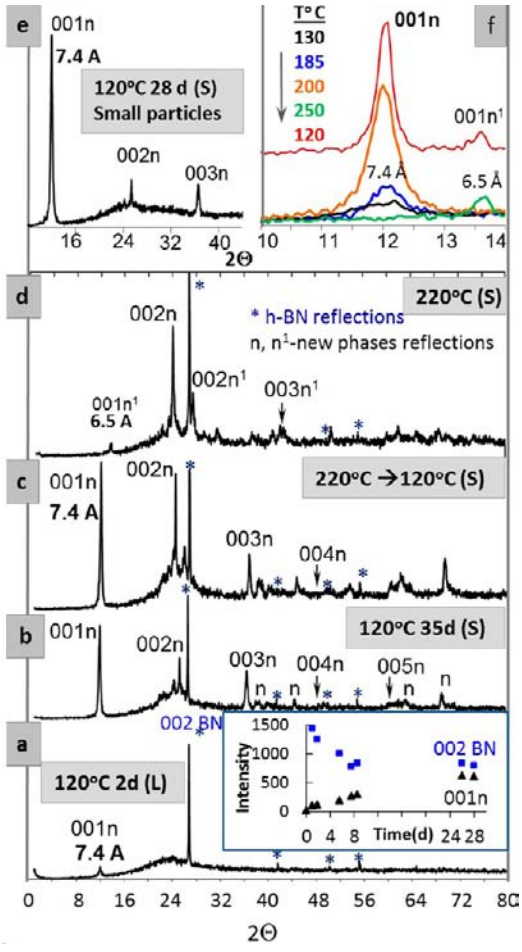

Figure 2. XRD patterns of h-BN/H_3PO_4 films prepared by (a) drying at 120 °C for 2 days (wet film (L) that shows the beginning of the intercalation process), (b) drying at 120 °C for 35 days (dry film (S), intercalation completed), (c) drying at 220 °C and then keeping at 120 °C for 24 days, (d) drying at 220 °C, and (e) drying at 120 °C for 28 days (dry film (S), sample area with mainly small particles) and (f) a sample that was kept at different temperatures: arrow shows the order of temperature change. (Inset in a) Intensity changes of the 002 BN and 001n reflections with time. Asterisk (*) indicates h-BN reflections; n, n^1 indicate reflections of the new phases.

dx.doi.org/10.1021/ja403197h | J. Am. Chem. Soc. 2013, 135, 8372−8381

BN/H_3PO_4 films. After their formation, the intercalation compounds are stable at the temperature of drying (90−130 °C, see Table S1, Supporting Information) or at ambient temperature in a dry atmosphere. Exposure to ambient air leads to gradual disappearance of the *00l* reflections of the intercalated phases, which reappear after reheating the samples at the drying temperatures (Figure 1a and 1b and inset). In the h-BN/H_2SO_4 system, another new phase with d_{001} = 8.2 Å forms under ambient conditions and persists after reheating (Figure 1b and inset). The 1.3 Å increase in the interlayer spacing upon cooling in air may indicate formation of hydrated sulfate species inside the h-BN matrix. Subsequent addition of the parent acid or water leads to complete disappearance of the intercalated phases.

In the h-BN/H_2SO_4 system, the intercalated phase becomes noticeable when the film appears completely dry (after several days of drying). In the case of h-BN/H_3PO_4 films, the intercalated phase appears considerably sooner (Figure 2a). When drying occurs at 120 °C, the *001* reflection of the intercalated phase becomes noticeable in ∼24 h and its intensity grows linearly for ∼7 days, after which the reaction slows down, judging from the relative intensities of reflections from the intercalated phase and h-BN (Figure 2a, inset). Interestingly, in some areas of the h-BN/H_3PO_4 film that are dominated by small h-BN particles, the original h-BN phase is completely absent from the XRD pattern (Figure 2e). Accordingly, in micro-Raman spectra (Figure S2, Supporting Information) recorded with the laser beam focused on the largest particles, the $(\nu_{B-N})/\nu_{s[P-(OH)3]}$ intensity ratio is much higher than it is in the spectra of smaller particles.

The stage-1 intercalation compound with an interlayer distance of d_{001} = 7.4 Å exists in the temperature range 120−200 °C. The XRD pattern of a sample heated at successively increasing temperatures shows this phase up to 200 °C (Figure 2 f). Heating this sample to 250 °C leads to disappearance of the 7.4 Å phase and formation of another intercalated phase with an interlayer spacing of 6.5 Å (Figure 2f). In a film prepared at 220 °C, only the 6.5 Å phase is observed (Figure 2d). (Although a reflection at 2θ = 24.04°, d = 3.7 Å, is also present, the most intense d_{001} reflection of the 7.4 Å phase is absent.) Cooling both samples to 120 °C results in reappearance of the 7.4 Å phase (Figure 2c and 2f). The XRD pattern of a sample first made at 220 °C and then cooled to and kept at 120 °C gradually becomes similar to that of the sample prepared at 120 °C, including in the high diffraction angle region.

This thermal reversibility is also observed by Raman spectroscopy (Figure 3b−d). The spectrum of the h-BN/H_3PO_4 film prepared at 120 °C contains many vibrations characteristic of orthophosphate species (Figure 3b), whereas that of the film prepared at 220 °C shows in addition the low-frequency vibrational modes of pyro- and polyphosphates (Figure 3d).[42−46] In the spectrum of a film prepared at 220 °C and then cooled to and kept at 120 °C, the polyphosphate features gradually disappear and the spectrum becomes similar to that of films prepared at 120 °C (Figure 3c). It is known that dehydration of H_3PO_4 results in polycondensation of the phosphate units, which can be reversed by exposure to water. Therefore, the reversible thermal dehydration/hydration of the phosphate species is most likely responsible for the structural transformations of the intercalated phases observed by XRD. This reversibility also implies the absence of covalent bonds to BN below 220 °C. Thus, acid molecules are held in the

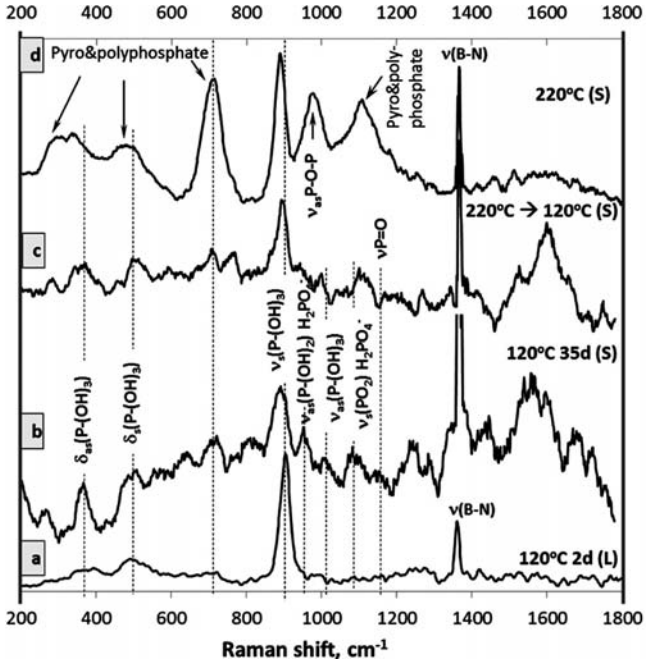

Figure 3. Raman spectra of h-BN/H_3PO_4 films prepared by drying at (a) 120 °C for 2 days (wet film that shows the beginning of the intercalation process in XRD patterns), (b) 120 °C for 35 days (dry film, intercalation completed), (c) at 220 °C and then keeping at 120 °C for 24 days, and (d) 220 °C.

interlayer galleries by noncovalent interactions. However at 250 °C, features characteristic of BPO_4 become noticeable in the XRD patterns and Raman spectra. Because the interlayer galleries in the intercalation compounds with H_3PO_4 narrow by 0.9 Å at higher temperatures and the intensities of the corresponding *00l* reflections decrease significantly, it is possible that H_3PO_4 polycondensation takes place on the outer surface of the h-BN host crystals and causes diffusion of the monophosphate species out of the galleries. In this scenario, the polyphosphate species rehydrate upon cooling, the concentration of the monophosphates increases, and they diffuse back into the interlayer galleries.

Electron microscopy images (Figure 4 a−g) reveal the morphology of the h-BN/H_2SO_4 (Figure 4a and 4d) and h-BN/H_3PO_4 (Figure 4b, 4e, and 4f) microcrystals, which is different from that of the starting h-BN powder (Figure 4c and 4g). In the dried h-BN/acid suspensions, the hexagonal and round crystal shapes of h-BN are much less pronounced and the crystals look thinner, more flexible, and partially delaminated (Figure 4f). Many of the h-BN/H_3PO_4 samples contain dense aggregates of the particles. Selected-area electron diffraction (SAED) patterns of h-BN/H_2SO_4 (Figure 4 a, inset) and h-BN/H_3PO_4 (Figure 4 b, inset) agree with the XRD patterns of new phases formed in these systems.

The composition of the h-BN/acid intercalation compounds was studied by energy-dispersive spectroscopy (EDS), X-ray photoelectron spectroscopy (XPS), and thermal analysis. EDS estimates of the sulfur content in h-BN/H_2SO_4 films prepared at 130 °C fell within the range of 1.0−9.5 atom % and differed considerably for different specimen locations (12 areas were measured). Thermal analysis (Figure S3, Supporting Information) revealed an average H_2SO_4 content of about 20 wt %, corresponding to ∼6 atom % of S, in reasonable agreement with the average of the EDS values. For the highest S

dx.doi.org/10.1021/ja403197h | J. Am. Chem. Soc. 2013, 135, 8372−8381

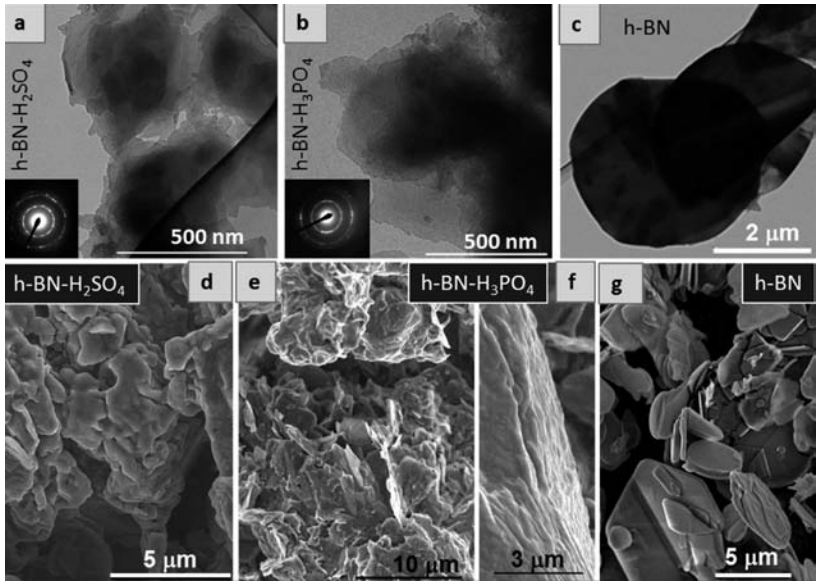

Figure 4. TEM (top) and FESEM (bottom) images of dry suspensions of (a and d) h-BN/H_2SO_4 and (b, e, f) h-BN/H_3PO_4 that were prepared at 130 and 120 °C, respectively, and show the intercalated h-BN phase in XRD patterns and (c and g) pristine h-BN powder. (f) Edge of a h-BN/H_3PO_4 crystal. Insets in a and b show SAED patterns.

concentration found (9.5 atom %) the BN/S atomic ratio is ~3.9, close to the composition of stage-1 graphite bisulfate, $C_{24}^{+}HSO_4^{-}(2H_2SO_4)$.[47] Importantly, EDS showed the highest sulfur content in samples made from the smallest (≤1 μm) h-BN particles, implying more complete diffusion into smaller h-BN crystals. As noted above, the same is true in the h-BN/H_3PO_4 system.

For h-BN/H_3PO_4 films prepared at 120 °C, EDS results were more homogeneous. P and BN contents were 20.1 atom % and 11.4 mol %, respectively (average of 16 specimen areas). The BN/P atomic ratio is 0.59. XPS analysis yields an N/P atomic ratio of 0.62, in good agreement with the EDS results. This value is clearly too low for a stage-1 intercalation compound, and formation of acid multilayers in the galleries is not supported by the XRD data (d_{001} = 7.4 Å). Therefore, we conclude that significant amounts of P-containing species must remain adsorbed on the external surface of the intercalation compounds.

Under the conditions of our experiments, accurate determination of the composition of the h-BN/H_2SO_4 and h-BN/H_3PO_4 intercalation compounds is difficult to achieve because dried suspensions contain significant amounts of intact h-BN (see XRD patterns in Figures 1 and 2) and because acid is adsorbed outside the galleries. It is known that the degree of intercalation of h-BN,[37] transition metal dichalcogenides, and graphite[1] depends strongly on the size and quality of the host crystals. In the present case, accurate determination of the intercalated acid content will require small, monodisperse h-BN crystals of good quality, which is a matter for future investigation.

SPECTROSCOPY AND STRUCTURE OF H-BN INTERCALATION COMPOUNDS

XPS. N 1s and B 1s core level spectra (Figure 5) of the h-BN/H_3PO_4 intercalation compound, compared with those of pristine h-BN powder (Figure 5 top right), reveal new components at higher and lower binding energies (BE) in both spectral regions. A new N 1s component appears at BE_{N1s}

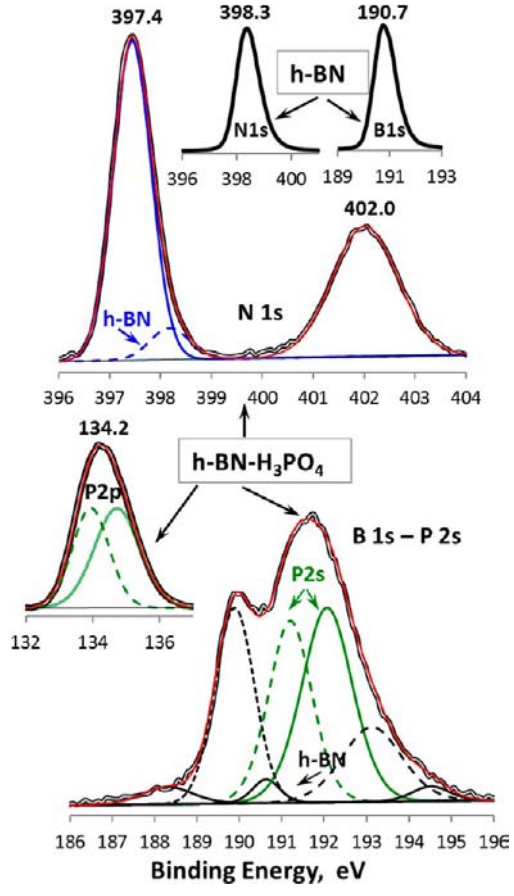

Figure 5. N 1s (top left), B 1s–P 2s (bottom right), and P 2p (bottom left) XPS spectra of a dry (120 °C) solid film of h-BN/H_3PO_4 and N 1s and B 1s (top right) spectra of pristine h-BN powder. All spectra were calibrated for BE_{C1s} = 285.0 eV (compound black curves are experimental spectra; red curves are curve-fitting envelopes; black, blue, and green curves are curve-fitting components of B, N, and P, respectively).

dx.doi.org/10.1021/ja403197h | J. Am. Chem. Soc. 2013, 135, 8372–8381

= 402 eV (Figure 5 top left). This value falls within the range of energies characteristic of protonated amine groups.[56,57] Another new N 1s component at BE = 397.4 eV is shifted by −0.9 eV relative to the N 1s peak of h-BN, suggesting the presence of N atoms with higher electron density in the h-BN/H_3PO_4 system.

Interpretation of the B 1s spectrum of the h-BN/H_3PO_4 film is complicated by partial overlap with the P 2s spectrum (Figure 5 bottom right). We estimated positions of the P 2s components in the B1s−P2s envelope using positions of the components in the P 2p spectrum (Figure 5 bottom left). The latter has an asymmetric shape and has to be fitted by at least two components with BE_{P2p} of ∼133.95 and ∼134.7 eV. For the phosphorus atom $BE_{P2s} - BE_{P2p} = 57.5 \pm 0.15$ eV.[58] Shifts in binding energies of a given atom that occur upon chemical conversion of one compound to another are the same for all of the inner orbitals.[59−61] This allows us to approximate the positions of the P2s components in the B 1s−P 2s envelope as ∼191.3 and ∼192.1 eV (Figure 5 bottom right, green lines). (The two components in the P 2p envelope are not assigned to any chemical species because of lack of XPS reference data. They serve only to approximate the positions of the P 2s components.) Other components required to fit the B 1s−P 2s envelope should be assigned to the B atoms (Figure 5 bottom right, black lines). As in the case of the N atoms, the B 1s binding energies suggest the occurrence of at least two types of boron atoms with higher and lower electron density relative to those of pristine h-BN.

In the h-BN/H_3PO_4 system, higher electron density on the B atoms may result from formation of P═O:→B dative bonds. This assignment is consistent with FTIR data (below) and literature on a shift of BE_{B1s} to lower energy in boron hydride complexes with electron-donor ligands.[62] The increase in electron density on the vacant p orbitals of boron should decrease the order of B−N bonds with the neighboring nitrogen atoms and increase the electron density on nitrogen. This may explain the lower binding energy N1s component at BE_{N1s} = 397.4 eV (Figure 8 top left, blue line). A decrease in the electron density on the nitrogen, which follows from the appearance of the higher binding energy N1s component at BE_{N1s} = 402.0 eV, may result from protonation or formation of strong hydrogen bonds, N···H···OP. This should decrease the B−N bond order with neighboring boron atoms and lower the electron density on boron. This is consistent with the occurrence of a higher binding energy B1s component at $BE_{B1s} \approx 193.7$ eV.

Vibrational Spectroscopy. Because intercalation of acids into the h-BN matrix becomes noticeable only after many hours of thermal drying of the h-BN/acid suspensions, the water content of the acid can decrease substantially during the reaction (Figure S4, Supporting Information). Therefore, acid spectra were taken after sulfuric and phosphoric acids were heated in air at 130 and 120 °C, respectively, for several hours, until water evolution almost stopped and their water contents remained approximately constant.

FTIR spectra of the concentrated aqueous acids (85% H_3PO_4 and 100% H_2SO_4) heated under the conditions of the intercalation reaction reveal bands characteristic of the H_3PO_4 molecule (Figures 6c and 7b) or the H_2SO_4 molecule and the HSO_4^- anion (Figures 6a and S3a, Supporting Information). HSO_4^- is formed by autodissociation of sulfuric acid[48] which may be enhanced by absorption of water during exposure of oleum (20%) to air at 130 °C. The broad band centered at

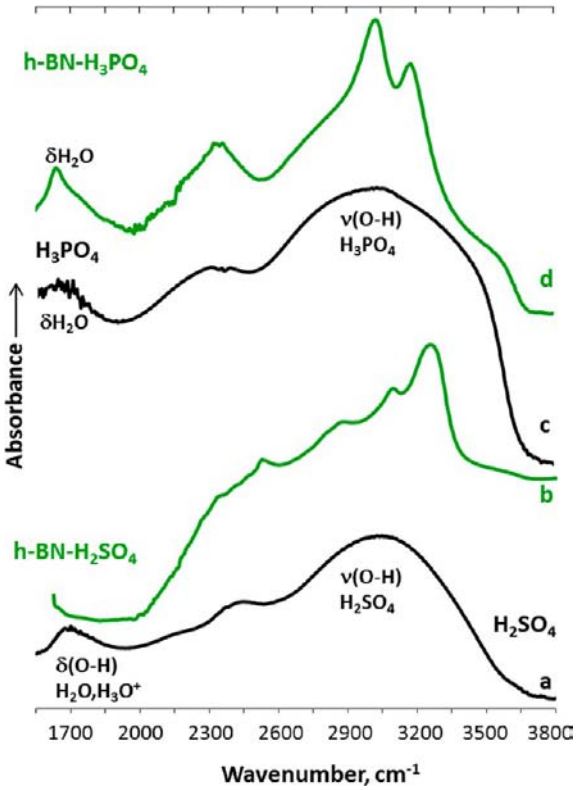

Figure 6. Transmission (a and c) and ATR (b and d) FT-IR spectra of (a) H_2SO_4−SO_3 20% heated at 130 °C for 3 h, (b) dry (130 °C) film of h-BN/H_2SO_4(ATR), (c) H_3PO_4 (85%) heated at 120 °C for 5 h, and (d) dry (120 °C) film of h-BN/H_3PO_4. Both dry films show h-BN intercalation phases in XRD.

∼1700 cm^{-1} can be assigned to superimposed $\delta(H_2O)$ and $\delta(H_3O^+)$ modes.[49] Full band assignments of the acid spectra were made according to the literature[42−44,48] and are shown in Figures 6 and 7and Figure S5 and Table S2, Supporting Information.

FTIR spectra of both acids revealed broad, continuous absorption bands in the O−H stretching region with maxima located near 3000, 2400, and 1650 cm^{-1} (Figure 6a and 6c). In concentrated acid solutions, this absorption continuum is characteristic of OH groups involved in a network of polarizable hydrogen bonds, such as P(S)OH···OP(S) and P(S)OH···OH_2.[50,51]

In the FTIR spectra of dried h-BN/acid films that contain the intercalated BN phase, the absorption intensity in the high-frequency continuum region decreases significantly and several new sharp maxima appear in the 2200−3400 cm^{-1} range (Figure 6 b and 6d). This is consistent with a decrease in polarizable hydrogen-bonding interactions,[51] which can occur if P(S)OH···OP(S) and P(S)OH···OH_2 bonds are disrupted by phosphate (sulfate) species and also if less polarizable H bonds are formed within the BN galleries. The shoulder at ∼3600 cm^{-1} indicates a higher concentration of the unassociated OH groups in the intercalation compound.[52]

In the mid-IR region, FTIR spectra of dried h-BN/H_3PO_4 films (Figure 7c and 7d) reveal two important differences from the spectra of H_3PO_4 (Figure 7b):

First, the $\nu_{(P=O)}$ band (formerly at 1135 cm^{-1}) broadens and reveals fine structure in the range 1100−1170 cm^{-1}. In the ATR spectrum (Figure 7d) there is a red shift of the band center by 43 cm^{-1} and a shoulder appears at ∼1160 cm^{-1}. A

dx.doi.org/10.1021/ja403197h | J. Am. Chem. Soc. 2013, 135, 8372−8381

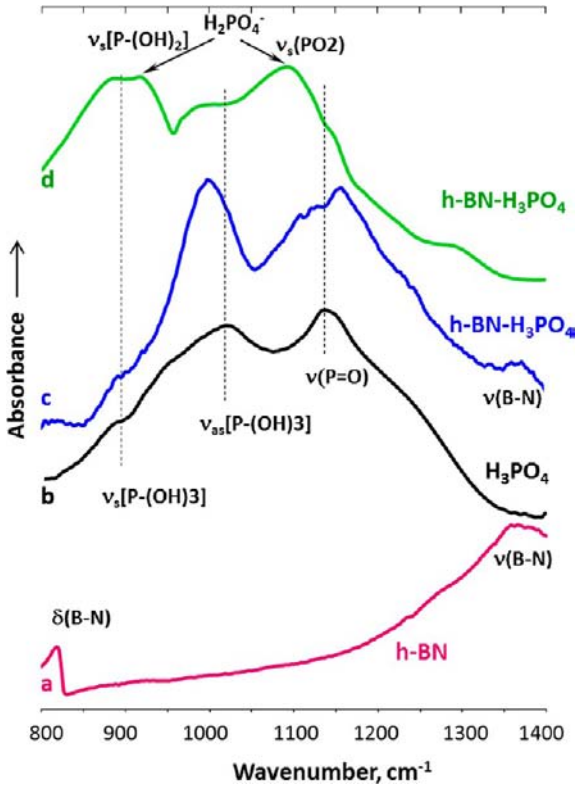

Figure 7. Transmission (a–c) and ATR (d) FT-IR spectra of (a) starting h-BN powder, (b) H_3PO_4 (85%) heated at 120 °C for 5 h, and (c and d) a dry (120 °C) film of h-BN/H_3PO_4. Dry film shows h-BN intercalation phases in XRD patterns.

similar splitting has been observed in metal–phosphine oxide complexes and assigned to nonequivalent ligands in the crystal.[52] The low-frequency component was explained by formation of a dative bond from the oxygen atom to a metal ion.[53−55] In the present case, lower frequency spectral features suggest formation of >P═O:→ $B^{\delta+}$ dative bonds between some of the acid molecules and the h-BN layers. The P═O groups of the other molecules may remain unbound and less involved in hydrogen bonding because of the low water content in the galleries; this would blue shift the $\nu_{(P=O)}$ band[46] and thus account for the higher frequency component. In the ATR spectrum, the position of the lower frequency component at 1092 cm^{-1} and the width of the band suggest the presence of the $H_2PO_4^-$ anion.[43,44] This is confirmed by the appearance of a Raman peak at ∼1083 cm^{-1}, Figure 3b.

Second, a new band appears at 917 cm^{-1}, or the $\nu_{s[P\text{-}(OH)3]}$ band at ∼890 cm^{-1} splits. This feature might be attributed to a blue shift of the $\nu_{s[P-\text{-}(OH)3]}$ mode of some of the acid molecules or to the $\nu_{as[P-(OH)2]}$ mode of the $H_2PO_4^-$ anion.[44] The latter is more likely because the $\nu_{as[P-(OH)3]}$ band red shifts by ∼20 cm^{-1}. (Some red shift of the $\nu_{s[P-(OH)3]}$ mode is also possible judging from the broadening of this band.) The Raman spectrum (Figure 3 b) also shows a red shift of the $\nu_{s[P-(OH)3]}$ mode and the appearance of the $\nu_{as[P-(OH)2]}$ mode of the $H_2PO_4^-$ anion. Here again it is important to recall that there are inequivalent H_3PO_4 molecules in the intercalation compound. While some acid molecules may form hydrogen bonds to the nitrogen atoms, P–OH···$N^{\delta-}$B, which are weaker than POH···O═P hydrogen bonds[46] (i.e., consistent with the $\nu_{[P-(OH)3]}$ mode shift to the lower frequencies), other H_3PO_4 molecules may dissociate by protonation of N atoms, $BNH^+\cdots H_2PO_4^-$. The Raman spectrum (Figure 3b) also shows new shifts at 1082 and 952 cm^{-1} that can be assigned to $\nu_{s[PO2]}$ and $\nu_{as[P-(OH)2]}$ modes, respectively, of to the $H_2PO_4^-$ anion.[43]

Raman spectra of h-BN/H_3PO_4 (S) films prepared at 120 °C (Figure 3 b and 3c) have a broad feature in the 1500–1650 cm^{-1} range, whose origin is not clear. Spectra of both the starting acid and the still-wet (dried for 2 days) h-BN/H_3PO_4 film (Figure 3a) are featureless in this region.

Comparison of the spectra of the H_2SO_4 precursor and the dried h-BN/H_2SO_4 film (Figure S4b and S4c, Supporting Information) reveals changes that are similar to those found for h-BN/H_3PO_4 (see Supporting Information for details). This suggests similar host–guest interactions in both systems. The following picture for both intercalation compounds emerges from the XPS and vibrational spectroscopic data.

- There is appreciable disruption of the acid–acid hydrogen bonds upon intercalation.
- There is evidence of dative bonds >P(S)═O:→$B^{\delta+}$ that are stronger in the h-BN/H_3PO_4 system because of the lower acidity of H_3PO_4.[50]
- There are hydrogen-bonding interactions between acidic OH groups and the nitrogen atoms of the sheets. Acid molecules also dissociate with partial protonation of nitrogen atoms in the BN layers. This appears more pronounced in h-BN/H_2SO_4, consistent with the higher acidity of H_2SO_4.
- There are two or more chemical environments for the acid molecules. The inequivalency may result from the presence of both adsorbed and intercalated acid molecules and/or different bonding interactions within the galleries.

In terms of theory and simulation, the precise equilibrium geometry and free energy balance of the intercalant system is a complex issue, due to the large, low-symmetry nature of the intercalant species, the unknown areal intercalant density, the possible role of residual water, and the free energy contributions from configurational entropy within the h-BN galleries and (for the purposes of establishing chemical potentials) the residual ambient solution. Often, experimental intercalant structures for such complex intercalants are disordered. Thus, we focus the calculations instead on thoroughly characterizing the range of possible intercalant geometries and thereby determine the favored generic local bonding interactions between the H_3PO_4 intercalant and the h-BN host, i.e., those that presumably drive intercalation. We follow a two-stage simulation strategy, beginning with a wide-ranging structural optimization at the level of empirical potentials (the ReaxFF reactive force field[64]) and then investigating key structures identified by this optimization in more detail at the density functional level.

We extensively searched the possible orientations of a single H_3PO_4 molecule inside an 8 × 8 h-BN supercell by inserting H_3PO_4 molecules at the midplane of a dilated h-BN gallery at random lateral positions and random molecular orientations. These initial geometries were briefly annealed and then relaxed into a local minimum, as described in the Experimental Section. Only those configurations in the lowest 10% in terms of binding energy were selected for further analysis; these are all sufficiently close to degenerate that all would be populated at room temperature. At the lowest areal density of one acid molecule per supercell, the H_3PO_4 molecules make an average

dx.doi.org/10.1021/ja403197h | J. Am. Chem. Soc. 2013, 135, 8372–8381

of two hydrogen bonds each to the nitrogen atoms of h-BN (Figure 8a-1 and 8b-1). A small fraction of the sampled

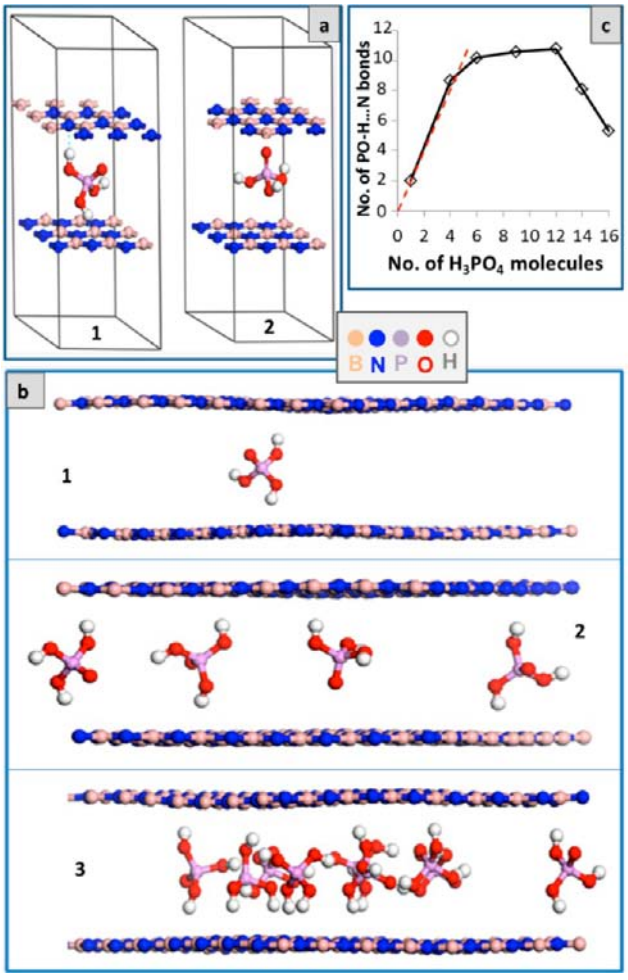

Figure 8. (a) Structural model of low-density H_3PO_4 molecules in a 3 × 3 h-BN supercell with periodic boundary conditions, relaxed using density functional theory. (b) Structure of phosphoric acid inside the h-BN gallery relaxed using empirical molecular dynamics with ReaxFF: (1) at a low density of one acid molecule per 8 × 8 BN supercell, (2) at a density of four H_3PO_4 molecules per supercell the acid molecules do not yet interact with each other, (3) at a density of nine phosphoric acid molecules per supercell the average number of PO−H···N hydrogen bonds per acid molecule is less than two. Acid molecules start clustering via formation of P—OH···O═P hydrogen bonds. (c) Average number of P−OH···N bonds as a function of the number of molecules in the supercell. Number of hydrogen bonds was obtained by counting hydrogen atoms within a cutoff distance from the h-BN layers. Dashed line has a slope of 2.

structures points their P═O group toward a BN sheet, slightly favoring the B site, which is consistent with formation of a P═O:→B dative bond (as described earlier in the discussion of XPS and vibrational spectra). Panel 2 of Figure 8b shows a typical outcome for an areal density of four H_3PO_4 molecules per supercell, showing the predominance of −OH···N hydrogen bonds and a slight admixture of P═O:→B interactions. At the highest phosphoric acid concentrations, the average number of −OH···N hydrogen bonds per acid molecule decreases as the acid molecules cluster via formation of —OH···O═P hydrogen bonds (Figure 8b, 3). Figure 8c depicts this trend in hydrogen bonding with intercalant density. When the areal density of acid molecules approaches that for crystalline solid H_3PO_4 packed into a similar gallery volume (approximately 16 acid molecules per supercell), hydrogen bonding is dominated by those between acid molecules.

To characterize acid−BN interaction at a more quantitative level, selected molecular orientations from the ReaxFF analysis were chosen for study within density functional theory (DFT) using a single H_3PO_4 molecule within a 3 × 3 bilayer h-BN supercell. This simplified unit cell clarifies analysis, at the cost of not describing more complex multi-intercalant clustering or sheet-crossing interactions. Initial structures were obtained from force-field-relaxed structures: four samples with hydrogen bonding to the BN layers and three samples with the oxygen in the P═O group close to the BN sheets. Calculations were performed in both the local density approximation and the generalized gradient approximation. All initial structures with hydrogen bonding to the h-BN sheet preserved this geometry upon relaxation within DFT (Figure 8a provides a representative example, showing two hydrogen bonds to N), but initial structures with P═O coordination suffered diverse fates: they preserved this geometry (with a preference for P═O sitting underneath B), but within the generalized gradient approximation (GGA) these systems relaxed to geometries more characteristic of hydrogen bonding. Considering the countervailing weaknesses of each method (the local density approximation (LDA) overestimates hydrogen-bond strength, whereas GGA underestimates certain nonbonded interactions), these outcomes are consistent with hydrogen bonding as the most important intercalant−host interaction with P═O:→B dative bonding playing a more minor role. It is possible that P═O:→B bonding interaction becomes more prevalent at higher intercalant densities, where acid−acid interactions become more important. The expanded *c* axis across the four hydrogen-bonded structures is 7.4−7.6 Å within LDA, which is consistent with the experimentally measured interlayer spacing of 7.4 Å. This agreement is encouraging, but one should not read too much into it, since the areal density of intercalant molecules in the stage-1 compounds is not known precisely.

Plausible Mechanism of h-BN Intercalation with Acids. The experimentally established steps of the redox-driven intercalation reactions of graphite and layered metal dichalcogenides are[26,63] (i) guest molecules adsorb on and transfer charge to the basal planes facilitating opening of the outer gallery, (ii) guests penetrate into the outermost interlayer galleries and activate the second (and successively other) outermost host layers, (iii) intercalation cascades from the edges of the outermost galleries into the bulk, (iv) the guest continues to diffuse into the host galleries until equilibrium is reached. Steps (i) and most likely (ii) are independent of guest concentration over a wide concentration range.[63] In contrast step (iii) occurs only after the guest concentration increases to a threshold value. The bulk intercalation compound appears after step (iii) as reflected in the XRD pattern.

Assuming a similar sequence of events for h-BN intercalation, but driven by acid−base rather than electron transfer reactions, one might also expect a concentration (or activity) threshold for formation of the intercalation compound in step (iii). However, the onset of bulk intercalation appears to be more complex in this case. Thermal analysis and FTIR data (see Supporting Information) show that 85% phosphoric acid initially dehydrates and maintains a constant composition (95.5% H_3PO_4) as long as the liquid phase is present in the wet h-BN film at the temperature of the intercalation reaction (120

dx.doi.org/10.1021/ja403197h | J. Am. Chem. Soc. 2013, 135, 8372−8381

°C). However, XRD patterns show no evidence of intercalation as long as excess liquid is present, and the intercalation compound appears only upon heating to dryness. This suggests that the acid molecules in the liquid phase cannot initiate intercalation, because of either kinetic or thermodynamic limitations, and that adsorbed acid molecules, or perhaps small clusters of molecules that are not part of the extensively hydrogen-bonded liquid, are the species that actually open and enter the h-BN galleries.

CONCLUSIONS

Thermal drying of suspensions of h-BN with sulfuric, perchloric, and phosphoric acids results in nonoxidative intercalation to form stage-1 compounds. The reaction is reversible, which is typical for intercalation of layered materials, and implies that no irreversible covalent bonds form to the BN layers. Reversible thermal hydration/dehydration of the guest species is the most likely reason for the reversible structural changes that occur.

XPS, vibrational spectroscopy, and thermal analysis data, together with DFT and molecular dynamics calculations, support a structural picture in which polar interactions between the guest molecules and the sheets drive the intercalation reaction. Specifically, there is evidence of interactions between >P(S)=O groups and boron atoms and between P(S)−OH groups and nitrogen atoms.

Under the conditions of our experiments with polydisperse h-BN powder, the intact h-BN phase is present in the system regardless of the h-BN/acid molar ratio and the yield of the intercalated phase depends on the fraction of smaller h-BN particles. This tendency has also been observed in the intercalation of graphite and transition metal dichalogenides.

EXPERIMENTAL SECTION

Materials. Boron nitride was purchased from UK Abrasives Inc. and used without any additional treatment. XRD, XPS, and FESEM data obtained for the starting powder are consistent with a pure h-BN phase composed of polydisperse (from ≤1 to ≥10 μm) good-quality crystals. No impurities were found. All acids, H_2SO_4–SO_3 (20%), H_3PO_4 (85%), $HClO_4$ (70%), HCl, HNO_3, CH_3COOH, HCOOH, and $C_6H_5SO_3H$, were commercial products of the highest available concentration and used as purchased. $C_6H_5SO_3H$ was used as 2.7 M aqueous solution.

Synthesis. A 70−200 mg amount of h-BN was added to 0.5−1 mL of acid in a glass vial, stirred with a glass stick, and allowed to settle. Excess acid (required to ensure complete wetting of the BN powder) was then decanted away. A drop of the remaining thick h-BN/acid suspension was cast on a glass or Si wafer and dried in air at a given temperature. For each acid, the drying temperature was chosen below its decomposition point but was high enough to enable drying within a reasonable period of time. h-BN suspensions with HCl, HNO_3, CH_3COOH, and HCOOH were dried at 25−40 °C and that with aq $C_6H_5SO_3H$ at 105 °C in vacuum. The range of drying temperatures for the h-BN suspensions with H_2SO_4 and H_3PO_4 is shown in Table S1, Supporting Information.

Characterization. As-prepared films were characterized by X-ray diffraction (XRD (Philips X'Pert MPD, Cu Kα radiation)), transmission electron microscopy (TEM), selected area electron diffraction (SAED, JEOL 1200 EXII, accelerating voltage 80 kV), and X-ray photoelectron spectroscopy (XPS, Kratos Analytical Axis Ultra, Al KR X-ray source). Spectra were acquired with a Kratos Axis Ultra using monochromatic Al Kα X-rays. Analysis chamber pressures were in the mid-10^{-8} Torr range during measurements. Pass energy was set at 20 eV, and step size was 0.1 eV for high-resolution scans. The high-resolutions scan dwell time was varied from 1000 to 2000 ms depending on the peak intensity. Under these conditions the P 2p doublet is represented as a single peak. XPS spectra were charge referenced to C1s at 285 eV. Micro-Raman spectroscopy used a Renishaw inVia confocal microscope-based Raman spectrometer with a laser excitation wavelength of 514.5 nm and laser spot ∼1 μm in diameter. Field emission scanning electron microscopy (FESEM) and energy-dispersive spectroscopy (EDS) were performed in low-vacuum mode using lacey carbon grids as substrates (FEI NanoSEM 630 FESEM, accelerating voltage 5 kV). Thermogravimetric (TG, 2050/Balzers ThermoStar 1−300 amu Mass Spectrometer) and differential thermal analyses (DTA, SDT 2960) were performed in Ar flow at a heating rate of 10 °C/min. Fourier transform infrared spectra (FT-IR) were collected in the transmittance mode with a Hyperion 3000 FT-IR Microscope. Scan area was 0.1 × 0.1 mm^2. A thin sample layer was deposited on a Si(100) substrate, which was kept at the temperature of synthesis (120−130 °C) to prevent water absorption during analysis. Attenuated total reflectance (ATR) spectra were collected with a diamond crystal with a 80 μm diameter contact surface.

Empirical Force Field and Density Functional Theory Modeling. Molecular dynamics annealing and relaxation were performed with the ReaxFF Reactive Force Field.[64] Parameters for H, O, C, and N atoms were taken from ref 65, phosphate parameters from refs 66 and 67, and B and N parameters from refs 68 and 69. Initial structures were composed of stacked h-BN layers separated by 7.5 Å and H_3PO_4 molecules distributed in between at varying densities, with their centers of mass fixed at the midplane of the galleries with random lateral positions and a uniform distribution of orientations. There were two h-BN layers in the 8 × 8 supercell with periodic boundary conditions. Seven areal densities of acid molecules were simulated, ranging from 1 to 16 acid molecules per 8 × 8 supercell. At the lowest areal density, 500 samples were generated (for better statistics to compare with density functional theory). At higher areal densities 100 initial structures were generated, followed by a brief nonreactive relaxation to remove unphysical overlaps between atoms. Samples were then annealed briefly at constant pressure starting at 800 K and cooled to 0 K within 2 ps, followed by a local structural relaxation including cell relaxation. The 500 relaxed samples with lowest acid molecule density (one per 8 × 8 supercell) were then examined to classify the acid molecule structure into two categories: those that were connected to the upper and lower BN sheets via at least one hydrogen bond on each side, and those that exposed the oxygen atom in the P=O group to BN. The 10 samples with the lowest energies at each density were analyzed further to characterize the density dependence of the hydrogen-bond distribution.

Density functional theory calculations were performed with the local density approximation (LDA) for the exchange-correlation functional as parametrized by Perdew and Zunger[70] and the generalized gradient approximation (GGA) functional parametrized by Perdew et al.[71,72] using projector-augmented wave (PAW) potentials,[73,74] as implemented by the Vienna Ab-initio Simulation Package (VASP).[75,76] Structural relaxations were performed with a *k*-point grid converged up to 4 × 4 × 2, with an electronic loop convergence threshold of 10^{-7} eV. Energy cutoff for the plane wave expansion was set to 400 eV, and ionic forces were converged to 0.01 eV/Å. The h-BN host lattice was preconverged without the phosphoric acid intercalant to remove pressure in the BN plane. To simplify analysis, structures with phosphoric acid intercalated between a 3 × 3 bilayer h-BN supercell were separated by 13 Å of vacuum in the direction perpendicular to the h-BN layers to eliminate interlayer interaction with periodic images and then relaxed with fixed cell parameters.

ASSOCIATED CONTENT

Supporting Information

Crystallographic data for BN intercalation compounds, thermal gravimetric data, Raman spectra, and infrared spectra. This material is available free of charge via the Internet at http://pubs.acs.org.

AUTHOR INFORMATION

Corresponding Author

E-mail: tem5@psu.edu; nina@chem.psu.edu; nanoprof@mac.com.

Notes

The authors declare no competing financial interest.

ACKNOWLEDGMENTS

Electron microscopy, FTIR, XPS, and thermal analyses were conducted at the Materials Characterization Laboratory of the Pennsylvania State University. We are grateful to Josh Stapleton and Vince Bojan for helpful discussions and acquiring the XPS spectra. We thank Yiyang Gong for help with the Raman experiments, and we thank Adri van Duin for assistance in developing the ReaxFF parametrization for description of the H_3PO_4/h-BN system. This work was supported by the U.S. Army Research Office MURI grant W911NF-11-1-0362.

REFERENCES

(1) In *Intercalated Layered Materials*; Levy, F., Ed.; D. Reidel: Dordrecht, 1979.

(2) In *Progress in intercalation research*; Muller-Warmuth, W., Schollhorn, R., Eds.; Kluwer: Dordrecht, 1994.

(3) Dresselhaus, M. S.; Dresselhaus, G. *Adv. Phys.* **2002**, *51*, 1−186.

(4) Sasaki, T.; Watanabe, M. *J. Am. Chem. Soc.* **1988**, *120*, 4682−4680.

(5) Li, D.; Muller, M. B.; Gilje, S.; Kaner, R. B.; Wallace, G. G. *Nat. Nanotechnol.* **2008**, *3*, 101−105.

(6) Luo, J.; Cote, L. J.; Tung, V. C; Tan, A. T. L.; Goins, P. E.; Wu, J.; Huang, J. *J. Am. Chem. Soc.* **2010**, *132*, 17667−17669.

(7) Park, S.; Ruoff, R. S. *Nat. Nanotechnol.* **2009**, *4*, 217−224.

(8) Chung, D. D. L. *J. Mater. Sci.* **1987**, *22*, 4190−4198.

(9) Mas-Ballesté, R.; Gómez-Navarro, C.; Gómez-Herrero, J.; Zamora, F. *Nanoscale* **2011**, *3*, 20−30.

(10) Wang, Q. H.; Kalantar-Zadeh, K.; Kis, A.; Coleman, J. N.; Strano, M. S. *Nat. Nanotechnol.* **2012**, *7*, 699−712.

(11) Geim, A. K.; Novoselov, K. *Nat. Mater.* **2007**, *6*, 183−191.

(12) Radisavljevic, B.; Radenovic, A.; Brivio, J.; Giacometti, V.; Kis, A. *Nat. Nanotechnol.* **2011**, *6*, 147−150.

(13) Song, L.; Ci, L.; Lu, H.; Sorokin, P. B.; Jin, C.; Ni, J.; Kvashnin, A. G.; Kvashnin, D. G.; Lou, J.; Yakobson, B. I.; Ajayan, P. M. *Nano Lett.* **2010**, *10*, 3209−3215.

(14) Gao, G.; Gao, W.; Cannuccia, E.; Taha-Tijerina, J.; Balicas, L.; Mathkar, A.; Narayanan, T. N.; Liu, Z.; Gupta, B. K.; Peng, J.; Yin, Y.; Rubio, A.; Ajayan, P. M. *Nano Lett.* **2012**, *12*, 3518−3525.

(15) Margulis, V. A.; Muryumin, E. E.; Gaiduk, E. A. *Physica B* **2012**, *407*, 4244−4250.

(16) Coleman, J. N.; Lotya, M.; O'Neill, A.; Bergin, S. D.; King, P. J.; Khan, U.; Young, K.; Gaucher, A.; De, S.; Smith, R. J.; Shvets, I. V.; Arora, S. K.; Stanton, G.; Kim, H.-Y.; Lee, K.; Kim, G.; Duesberg, G.; Hallam, T.; Boland, J.; Wang, J.; Donegan, J.; Grunlan, J.; Moriarty, G.; Shmeliov, A.; Nicholls, R.; Perkins, J.; Grieveson, E.; Theuwissen, K.; McComb, D.; Nellist, P.; Nicolosi, V. *Science* **2011**, *331*, 568−571.

(17) Smith, R. J.; King, P.; Loty, M.; Wirtz, C.; Khan, U.; De, S.; O'Neill, A.; Duesberg, G.; Grunlan, J.; Moriarty, G.; Chen, J.; Wang, J.; Minett, A.; Nicolosi, V.; Coleman, J. N. *Adv. Mater.* **2011**, *23*, 3944−3948.

(18) Zeng, Z.; Sun, T.; Zhu, J.; Huang, X.; Yin, Z.; Lu, G.; Fan, Z.; Yan, Q.; Hng, H. H.; Zhang, H. *Angew. Chem., Int. Ed.* **2012**, *51*, 9052−9056.

(19) Zhou, K.-G.; Mao, N.-N.; Wang, H.-X.; Peng, Y.; Zhang, H-L.. *Angew. Chem., Int. Ed.* **2011**, *50*, 10839−10842.

(20) Oyler, K. D.; Ke, X. L.; Sines, I. T.; Schiffer, P.; Schaak, R. E. *Chem. Mater.* **2009**, *21*, 3655−3661.

(21) Joensen, P.; Frindt, R. F.; Morrison, S. R. *Mater. Res. Bull.* **1986**, *21*, 457−461.

(22) Li. X. Zhang, G.; Bai, X.; Sun, X.; Wang, X.; Wang, E.; Dai, H. *Nat. Nanotechnol.* **2008**, *3*, 538−542.

(23) Kovtyukhova, N. I.; Ollivier, P. J.; Martin, B. R.; Mallouk, T. E.; Chizhik, S. A.; Buzaneva, E. V.; Gorchinskiy, A. D. *Chem. Mater.* **1999**, *11*, 771−778.

(24) Valles, C.; Drummond, C.; Saadaoui, H.; Furtado, C. A.; He, M.; Roubeau, O.; Ortolani, L.; Monthioux, M.; Pénicaud, A. *J. Am. Chem. Soc.* **2008**, *130*, 15802−15804.

(25) Hannes, C.; Li, J.-L.; McAllister, M. J.; Sai, H.; Herrera-Alonso, M.; Adamson, D. H.; Prud'homme, R. K.; Car, R.; Saville, D. A.; Aksay, I. A. *J. Phys. Chem. B* **2006**, *110*, 8535−8539.

(26) McKelvy, M.; Glaunsinger, W. *Annu. Rev. Phys. Chem.* **1990**, *41*, 497−523.

(27) Schollhorn, R. *Comments Inorg. Chem.* **1983**, *2*, 271−292.

(28) Levendorf, M. P.; Kim, C.-J.; Brown, L.; Huang, P. Y.; Havener, R. W.; Muller, D. A.; Park, J. *Nature* **2012**, *488*, 627−632.

(29) Dean, C. R.; Young, A. F.; Meric, I.; Lee, C.; Wang, L.; Sorgenfrei, S.; Watanabe, K.; Taniguchi, T.; Kim, P.; Shepard, K. L.; Hone, J. *Nat. Nanotechnol.* **2010**, *5*, 722−726.

(30) Siria, A.; Poncharal, P.; Biance, A.-L.; Fulcrand, R.; Blase, X.; Purcell, S. T.; Bocquet, L. *Nature* **2013**, *494*, 455−458.

(31) Chang, C. W.; Okawa, D.; Majumdar, A.; Zettl, A. *Science* **2006**, *314*, 1121−1124.

(32) Watanabe, K.; Tanigushi, T.; Kanda, H. *Nat. Mater.* **2004**, *3*, 404−409.

(33) Doll, G.; Speck, J.; Dresselhaus, G.; Dresselhaus, M.; Nakamura, K.; Tanuma, S. *J. Appl. Phys.* **1989**, *66*, 2554−2558.

(34) Hoffman, D.; Doll, G.; Eklund, P. *Phys. Rev. B* **1984**, *30*, 6051−6056.

(35) Sakamoto, M.; Speck, J.; Dresselhaus, M. *J. Mater. Res.* **1986**, *1*, 685−692.

(36) Hooley, J. S. Elements. In *Preparation and Crystal Growth of Materials with Layered Structure*; Lieth, R. M. A., Ed.; D. Reidel: Dordrecht, 1977.

(37) Hooley, J. S. *Carbon* **1973**, *11*, 225−236.

(38) Sumiyoshi, A.; Hyodo, H.; Kimura, K. *J. Phys. Chem. Solids* **2010**, *71*, 569−571.

(39) Shen, C.; Mayorga, S.; Biagioni, R.; Piskoti, C.; Ishigami, M.; Zettl, A.; Bartlett, N. *J. Solid State Chem.* **1999**, *147*, 74−81.

(40) Oba, F.; Togo, A.; Tanaka, I.; Watanabe, K.; Taniguchi, T. *Phys. Rev. B* **2010**, *81*, 075125.

(41) Zhang, Z.; Guo, W. *J. Phys. Chem. Lett.* **2011**, *2*, 2168−2173.

(42) Socrates, G. *Infrared and Raman characteristic group frequencies*; J. Wiley & Sons: New York, Chichester, 2001; Chapters 16, 17, 22.

(43) Rudolph, W. *Dalton Trans.* **2010**, *39*, 9642−965.

(44) Chapman, A. C.; Thirlwell, L. E. *Spectrochim. Acta* **1964**, *20*, 937−947.

(45) Bellamy, L. *The Infra-Red Spectra of Complex Molecules*; Chapman and Hall: London, 1975.

(46) Corbridge, D. *Phosphorus. An outline of its chemistry, biochemistry and uses*; Elsevier: Amsterdam, 1995; Chapters 3, 13, 14.

(47) Bottomley, M.; Parry, G.; Ubbelohde, A.; Young, D. *J. Chem. Soc.* **1963**, 5674−5680.

(48) Giguere, P.; Savoie, R. *Can. J. Chem.* **1960**, *38*, 2467−2476.

(49) Falk, M.; Giguere, P. *Can. J. Chem.* **1957**, *35*, 1195−1204.

(50) Leuchs, M.; Zundel, G. *Can. J. Chem.* **1979**, *57*, 487−493.

(51) Janoschek, R.; Weidemann, E. G.; Zundel, G.; Pfeiffer, H. *J. Am. Chem. Soc.* **1972**, *94*, 2387−2396.

(52) Nakamoto, K. *Infra-Red and Raman Spectra of Inorganic and Coordination Compounds*; J. Wiley & Sons: New York, 1997.

(53) Cotton, F.; Barnes, R.; Bannister, E. *J. Chem. Soc.* **1960**, 2199−2203.

(54) Goodgame, D.; Cotton, F. *J. Chem. Soc.* 1961, 2298-2305 (1961).

(55) Sheldon, J.; Tyree, S. *J. Am. Chem. Soc.* **1958**, *80*, 4775−4778.

(56) Beamson, G.; Briggs, D. *High-Resolution XPS of Organic Polymers: the Scienta ESCA300 database*; Wiley: Chichester, 1992.

(57) Moulder, J. F.; Stickle, W. F.; Sobol, P. E.; Bomben, K. D. *Handbook of X-ray Photoelectron Spectroscopy*; Perkin-Elmer Co.: 1992.

(58) Swift, P. *Surf. Interface Anal.* **1982**, *4*, 47−51.
(59) Morgan, W.; Van Wazer, J.; Stec, W. *J. Am. Chem. Soc.* **1973**, *95*, 751−755.
(60) Stec, W.; Morgan, W.; Albridge, R.; Van Wazer, J. *Inorg. Chem.* **1972**, *11*, 219−225.
(61) Jolly, W.; Hendrickson, D. *J. Am. Chem. Soc.* **1970**, *92*, 1863−1871.
(62) Il'inchik, E.; Volkov, V.; Mazalov, L. *J. Struct. Chem.* **2005**, *46*, 523−534.
(63) Wang, C.; McKelvy, M.; Glaunsinger, W. *J. Phys. Chem.* **1996**, *100*, 19218−19222.
(64) van Duin, A. C. T.; Dasgupta, S.; Lorant, F.; Goddard, W. A., III *J. Phys. Chem. A* **2001**, *105*, 9396−9409.
(65) Rahaman, O.; van Duin, A. C. T.; Goddard, W.A.;, III; Doren, D. J. *J. Phys. Chem. B* **2011**, *115*, 249−261.
(66) Abolfath, R. M.; van Duin, A. C. T.; Biswas, P.; Brabec, T. *J. Phys. Chem. A* **2011**, *115*, 11045−11049.
(67) Zhu, R.; Janetzko, F.; Zhang, Y.; van Duin, A. C. T.; Goddard, W. A.; Salahub, D. R. *Theor. Chem. Acc.* **2008**, *120*, 479−489.
(68) Weismiller, M. R.; Russo, M. F.; van Duin, A. C. T.; Yetter, R. A. *Proc. Combust. Inst.* **2013**, *34*, 3489−3497.
(69) Weismiller, M. R.; van Duin, A. C. T.; Lee, J.; Yetter, R. A. *J. Phys. Chem. A* **2010**, *114*, 5485−5492.
(70) Perdew, J. P.; Zunger, A. *Phys. Rev. B* **1981**, *23*, 5048.
(71) Perdew, J. P.; Burke, K. *Phys. Rev. Lett.* **1996**, *77*, 3865.
(72) Perdew, J. P.; Burke, K.; Ernzerhof, M. *Phys. Rev. Lett.* **1977**, *78*, 1396.
(73) Kresse, G.; Fürthmuller, J. *Phys. Rev. B* **1996**, *54*, 11169.
(74) Kresse, G.; Fürthmuller, J. *Comput. Mater. Sci.* **1996**, *6*, 15.
(75) Blöchl, P. E. *Phys. Rev. B* **1994**, *50*, 17953.
(76) Kresse, G.; Joubert, J. *Phys. Rev. B* **1999**, *59*, 1758.